

A 5kHz Modulator for Pyramid Wavefront Sensors

Maximilian Häberle ^{1,2*}, Vianak Naranjo¹, Yared Reinartz ¹,
Markus Feldt ¹, Silvia Scheithauer ¹, Thomas Bertram ¹,
Arne Bramigk³, Harry Marth³

¹Max Planck Institute for Astronomy (MPIA), Königstuhl 17, 69117 Heidelberg, Germany.

²European Southern Observatory, Karl-Schwarzschild-Straße 2, 85748 Garching, Germany.

³Physik Instrumente (PI) SE & Co. KG, Auf der Römerstraße 1, 76228 Karlsruhe, Germany.

* Corresponding author(s). E-mail(s): haeberle@mpia.de;

Abstract

Despite the emergence of new types of wavefront sensors, the modulated pyramid wavefront sensor remains the workhorse for ELT instrumentation, and is among the options even for advanced high-contrast, high-Strehl instrumentation like PCS and SAXO+. To achieve the required degree of wavefront control, an operation at frequencies of 3kHz, ideally up to 5kHz, is necessary, requiring an optomechanical device capable of delivering accurate circular modulation patterns with these frequencies. Here, we present tests of a novel type of high-frequency modulator based on shearing piezo actuators. The modulator prototype moves a flat circular mirror (15mm diameter) with a tip-tilt range of plus/minus 50 arcsec. At a typical 10mm pupil diameter on the modulator mirror, and operating at 2.2 μ m, this will create a modulation circle with a radius of slightly greater than $2\lambda/D$. While this is less than conventionally specified for most instruments, it should already be sufficient for any practical application except for very bad conditions or extended targets. We performed modulation tests at frequencies between 250 Hz to 5 kHz using a test setup including a modulated laser beam probed with a high-speed camera. The prototype showed stable behaviour during a one-hour-long operation at a maximum frequency of 5 kHz and with negligible heat generation. The maximum modulation amplitude was 60 arcsec. We observed very accurate reproduction of the input modulation pattern with typical ellipticities less than 1% and random deviations below 0.2% for frequencies below 4.5 kHz. These tests demonstrate the prototype's capabilities and could be followed by on-sky tests or the integration of the modulator into XAO testbeds.

Keywords: high frequency modulator, pyramid wavefront sensors, Adaptive Optics, ELT

1 Introduction

Adaptive optics (AO) have enabled diffraction-limited observations with ground-based telescopes, leading to various breakthroughs in our astrophysical understanding of the universe (Davies and Kasper 2012), from high-resolution studies of the Galactic Center (e.g. Gillessen et al. 2017) to direct observations of exoplanets (e.g. Chomez, A. et al. 2025). With future instruments and even larger telescopes, the requirements on AO systems are continuously evolving. In particular the direct observation of exoplanets, poses the most demanding requirements on AO systems. The need to suppress the light of a planet’s host star to detect the planetary source, 10^5 to 10^9 times fainter, at separations only a couple of times larger than the theoretical diffraction limit of the telescopes, requires the wavefront entering the instrument to be controlled - and thus determined - down to levels of a few tens of nanometers. To achieve such a degree of control, measuring and correcting at dense spatial and temporal sampling is required.

One key component of every AO system is its wavefront sensor (WFS), which measures the shape of the incoming wavefront and provides the feedback for the closed-loop control systems. Many current and near-future AO systems use so-called Pyramid Wavefront Sensors (PWFSs) (Ragazzoni 1996). While alternative sensor types, such as the Bi-O-edge (Vérinaud et al. 2024), the Zernike-sensor (N’Diaye et al. 2024), or the more elaborate concepts for coronagraphic wavefront sensors (Chambouleyron et al. 2024) are emerging and slowly making their way from theory via lab experiments to on-sky operation, the PWFS remains the workhorse for the near-future generation of ELT instruments (Feldt et al. 2024; Clénet et al. 2022; Bond et al. 2024), and an important fallback solution for the next generation.

1.1 Pyramid wavefront sensors and the need for modulation

The concept of the PWFS was introduced by Ragazzoni (1996). At the time, the standard WFS in use for astronomical AO systems was the Shack-Hartmann wavefront sensor (SHWFS) (Hartmann 1900). The PWFS has a higher sensitivity than the SHWFS, in particular in the low flux regime, and at low spatial frequencies (Vérinaud et al. 2005). The downside is a limited linear range when compared to the SHWFS. This downside can be overcome by means of a mechanical modulation device in the form of a tip-tilt mirror at the expense of some of the sensitivity gains (Burvall et al. 2006). The task of the tip-tilt mirror is to move the PSF image, which in the original concept falls onto the vertex of the four-sided pyramid prism, around said vertex on a full circle once during each integration cycle. By adjusting the radius of the circle, the so-called modulation amplitude, one can adjust the sensitivity of the sensor versus the linear range: High modulation amplitudes essentially make the PWFS equivalent to the SHWFS, low amplitudes or no modulation at all render the PWFS a very sensitive phase sensor with a very limited dynamic range. For so-called eXtreme AO (XAO) applications in the context of exoplanet imaging, it is usually found that a modulation amplitude between 2 and $4 \lambda/D$ is ideal, λ being the wavelength at which the sensor is operating, and D the diameter of the telescope’s primary mirror

One current example for such an XAO instrument at the forefront of technological development is the SAXO+ upgrade [Boccaletti et al. \(2022\)](#) for the SPHERE high-contrast instrument. It will equip the instrument with a fast second stage AO that will use a PWFS and will run at frequencies of up to 3 kHz with an ideal modulation amplitude of $2\lambda/D$ (see [Goulas et al. 2024](#), for detailed performance simulations). SAXO+ is also regarded as a mandatory technology demonstrator for the future Planetary Camera and Spectrograph (PCS) at the European Southern Observatory’s Extremely Large Telescope. To achieve the necessary wavefront quality, PCS will also use a multistage AO with an even higher sampling rate of up to 4 kHz ([Kasper et al. 2021](#)). While SAXO+ is already in the stage of manufacturing and system assembly, the currently foreseen modulation solution for the PWFS, based on a Physik Instrument (PI) S331 actuator ([Schatz et al. 2022](#), e.g.) in combination with a custom controller, still needs to be verified at high frequencies, and the final achievable frequency is not yet known. A discussion of the requirements for the SAXO+ modulator in context of the tested prototype is given in [Section 5](#).

PCS on the other hand is in a very early stage, where not even full end-to-end simulations yet exist, and a choice of WFS type cannot be made. Nevertheless, the evidence of the significant challenge frequencies above 1.5 kHz, let alone the aforementioned 4 kHz pose, led to a preliminary exclusion of the PWFS type, which can now be reconsidered.

Apart from alternative sensor concepts, modulation-less solutions are also under investigation for PWFSs, see e.g. [Ragazzoni et al. \(2002\)](#), [Costa et al. \(2003\)](#), [Hutterer and Ramlau \(2018\)](#), [Guzmán et al. \(2024\)](#), and [Landman et al. \(2025\)](#). Nevertheless, having a modulation device capable of delivering reliable modulation at up to 4 kHz remains highly desirable, as it would allow the continued operation of the well-proven PWFS concept, of which various instances are in use every night at observatories around the globe, in future planet-hunting XAO systems.

Laboratory experiments that test very fast control loops are e.g. the LLAMAS experiment ([Ammons et al. 2018](#)) or the GHOST testbench ([Engler et al. 2022](#)).

1.2 Outline

In this paper, we describe tests performed on a new high-frequency modulation device capable of modulation frequencies of 5 kHz. In [Section 2](#) we describe the prototype device itself. In [Section 3](#) we describe the optical setup used to test the new modulator. [Section 4](#) describes the data reduction and the results of the modulation performance tests. We conclude the paper with a summary ([Section 5](#)) and possible next steps in [Section 6](#).

2 Description of the modulation device

The high-frequency modulator prototype was designed and built by Physik Instrumente (PI) in Karlsruhe. The basic specifications are given in [Table 1](#). A design with four piezo actuators was chosen to achieve the required high dynamics. These are arranged in a $4 \times 90^\circ$ circle, with the opposite actuators being controlled in push-pull

Table 1 Specifications of the modulator prototype

External dimensions:	$40 \times 40 \times 18 \text{ mm}^3$
Mirror dimensions:	$\varnothing 15 \text{ mm} \times 3 \text{ mm}$
Max. Tip-Tilt angles:	$\pm 34 \text{ arcsec}$ at $\pm 500 \text{ V}$
Resonance frequency:	9.8 kHz

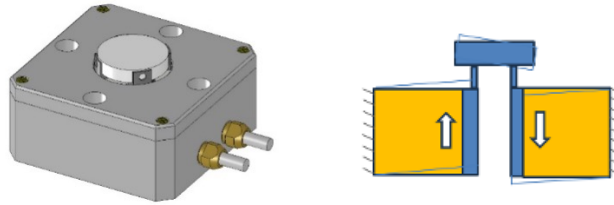


Fig. 1 *Left:* 3D Design drawing of the high-frequency modulator prototype. *Right:* 2D Schematic showing the push-pull actuation principle.

mode (see [Figure 1](#)). This results in a counter-rotating movement of the actuators and the desired tilting movement of the mirror platform in two orthogonal axes.

The piezo actuators are manufactured in a stacked design from PIC050 piezoelectric material (PI Ceramic). This crystalline material exhibits excellent linearity of deflection with negligible hysteresis, meaning that in many cases a position sensor is not required and open-loop operation is possible. A shear actuator was chosen as the design. The electro-mechanical coupling of the piezoelectric shearing mode is highly efficient, enabling a compact design that meets the desired stroke, with high stiffness to promote good dynamical properties.

Piezo actuators made of PIC050 behave electrically like capacitors with very low capacitance and low dielectric loss factors. The Reactive power does not heat up the actuators and allows continuous operation at high frequencies. The above application has been tested for continuous operation up to 5 kHz without significant heating of the mechanics.

3 Measurement setup

3.1 Optical setup

To verify the performance of the modulator at high frequencies at MPIA, we used a test setup in which we tracked the path of a LASER beam deflected by the HF modulator using a highspeed camera. An overview of the different components that were all mounted on an optical table is given in [Figure 2](#). A description of the different optical components (in the order they appear in the light path) is given in the following.

1. A 1mW HeNE LASER (Manufacturer: Melles-Griot) with a $\times 30$ beam expander is used as light source and produces a collimated beam of width of approximately 30 mm.

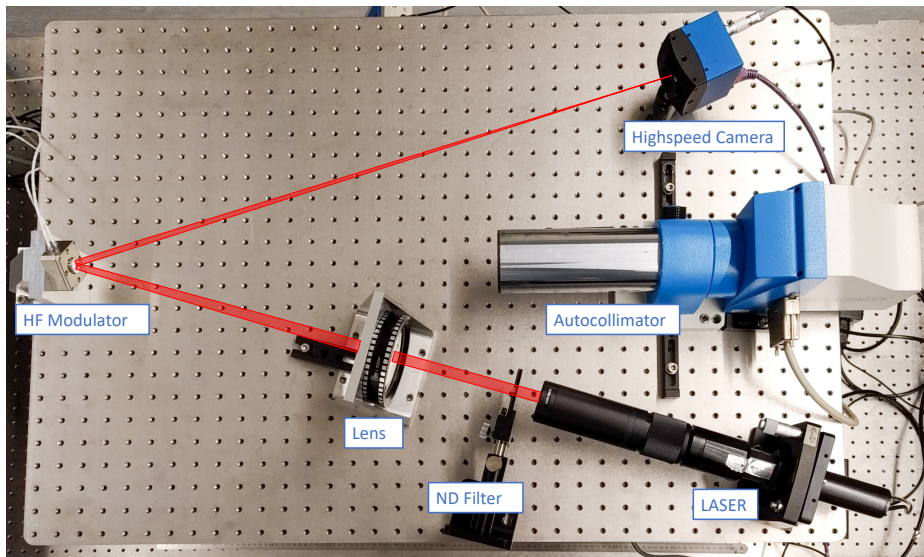


Fig. 2 Overview of the test setup mounted on an optical table. All components are labeled. The path of the laser beam is indicated in red.

2. The light is attenuated by 99.99% using a combination of neutral-density (ND) filters to avoid saturating the camera.
3. A lens with a focal length of $f = 1000$ mm is used to focus the beam on the detector of the camera
4. The converging light beam falls on the modulator, which has a movable, circular mirror with a diameter of 15mm. The light is reflected with the commanded tip-tilt offset.
5. The focused light finally falls on the sensor of a high-speed camera (*Mikroton MotionBLITZ EoSens mini2*) which is continuously read out at high frequency to record the modulation patterns.

3.2 Measurement process to characterize the modulation pattern

To command the modulator, a 2-channel frequency generator (*KEYSIGHT 33600A Series*) is connected to a high-voltage amplifier¹, that produces the high-voltage necessary to drive the two axes of the modulator. In order to produce a circular modulation pattern, we command the modulator with two identical sinusoidal signals shifted by 90° . To study the behaviour at different frequencies and amplitudes, we conduct a sweep through 20 different frequencies (from 250 Hz to 5000 Hz in steps of 250 Hz) and 10 different amplitudes (with the amplifier input signal ranging from $1 V_{pp}$ to $10 V_{pp}$

¹Amplifier model: *Physik Instrumente: E-508K026*, Voltage amplification: $\times 100$

in steps of 1 V. The output voltage of the amplifier therefore ranged from $100 V_{pp}$ to $1000 V_{pp}$.

At each frequency-amplitude combination, we record a series of 1000 images with the highspeed camera. The camera is read out at a frame rate of 36899 Hz and with a shuttertime of $3 \mu s$, meaning that each recorded sequence has a length of around 0.027 s. To achieve the high frequencies, a region of interest of 144×122 pixels is used, enough to capture the full modulated circle even at the highest amplitudes.

3.3 Calibration of modulator angles using an autocollimator

To find the precise relation between modulator angles and recorded positions of the modulated LASER beam on the camera sensor, we probe the angle of the modulator mirror at different constant input voltages with an autocollimator (*Möller-Wedel ELCOMAT 3000*), while simultaneously saving the readout of the camera. The autocollimator measurements are performed relative to the resting position of the modulator, i.e. when 0 V are applied to both axes.

We used different input voltages covering the full specified range of the modulator (i.e. from $-5 V$ to $5 V$ in both axes). An illustration of this process is shown in [Figure 3](#). Measured angles ranged from ± 50 arcsec, exceeding the specified range (see [Table 1](#)). We then use a least-square fit to determine the optimal affine transformation between pixel coordinates and angles. Using an affine transformation is necessary, as a slight misalignment of the camera sensor can lead to a shearing and therefore apparent ellipticity of the modulation pattern. The affine transformation can be described with a partially populated 3×3 matrix or with 6 explicit parameters. The explicit form as implemented in `scikit.image` ([van der Walt et al. 2014](#)) is:

$$x' = s_x \cdot x \cdot (\cos \theta) - s_y \cdot y \cdot (\sin \theta + \tan h \cdot \cos \theta) + t_x \quad (1)$$

$$y' = s_x \cdot x \cdot (\sin \theta) - s_y \cdot y \cdot (\tan h \cdot \sin \theta - \cos \theta) + t_y \quad (2)$$

with the scale factors s_x and s_y , the rotation angle θ , the shear value h , and the translations t_x and t_y . The best fit transformation shows minimal rotation ($\theta = 0.12^\circ$) and a mean scale of $\frac{1}{2}(s_x + s_y) = 1.26$ arcsec/pixel. This is matching our expectation: The high-speed camera pixels have a size of $8 \mu m$ and are at a distance of around 66 cm from the modulator mirror, leading to an expected scale of 1.25 arcsec/pixel. The residuals of our transformations show a root mean square of 0.17 arcsec, which is within the nominal accuracy of the autocollimator (± 0.25 arcsec). We note that while the calibration delivers the absolute scale of our measurements, it does not significantly influence the achievable accuracy of the (relative) high-frequency tests.

3.4 Test of sound emission

At higher frequencies (> 2000 Hz) the modulator produces a noticeable (and eventually disturbing) sound. We measured the acoustic signal with a sound level meter (*VOLTCRAFT Schallpegelmessgerät 320*), mounted approximately 75 cm above the

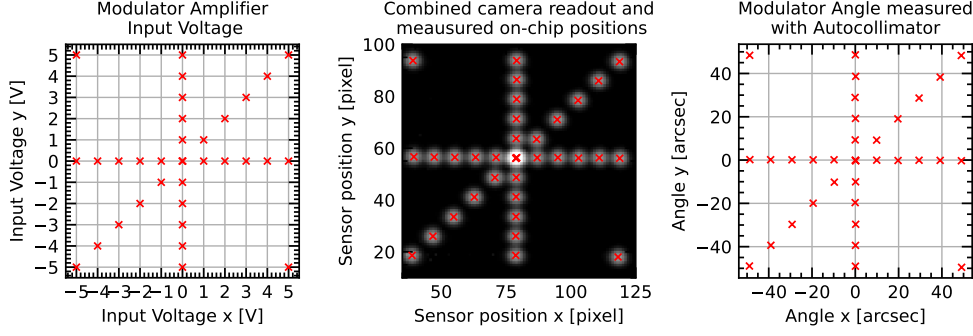


Fig. 3 This figure illustrates the three stages of the calibration process. The left panel shows the commanded input voltages, covering the full range used during the modulator operation. The center panel shows the combined readout of the highspeed camera, the laser spot at different positions is clearly visible. Finally the right panel shows the corresponding modulator angles, directly measured with the autocollimator.

optical bench. The modulator was run at the highest possible amplitude ($10 V_{pp}$) and with frequencies between 250 Hz and 7000 Hz. The measured sound levels showed an increase with frequency, and reached a level of around 80 dB at frequencies ≥ 5 kHz. We note that the acoustic tests were performed in an optical laboratory without any mitigation of possible acoustic echoes or resonances and are therefore of a qualitative nature.

3.5 Measurement of long term stability and heat-generation

To test the long-term stability during operation of the modulator, we ran it continuously for 1 hour with a modulation frequency of 5000 Hz and at an input amplitude of $10 V_{pp}$. At the same time we recorded the temperature of the modulator housing using a DT-670 temperature sensor. Figure 4 shows how the measured temperature of the modulator housing evolved with respect to the mean temperature of two other temperature sensors placed at different locations in the laboratory. Only very minor temperature fluctuations (full range: $\Delta T = 0.04$ K) were observed. The measured fluctuations were significantly lower than the overall temperature fluctuations within the laboratory.

4 Data reduction and results

4.1 Data reduction

The goal of this step is to derive the properties of the modulation pattern from the image sequences recorded for different modulator frequencies and amplitudes. An illustration of this process is given in Figure 5.

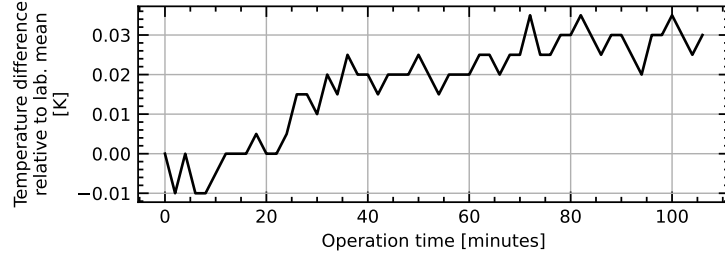


Fig. 4 Change of the modulator housing temperature relative to the mean temperature of the laboratory.

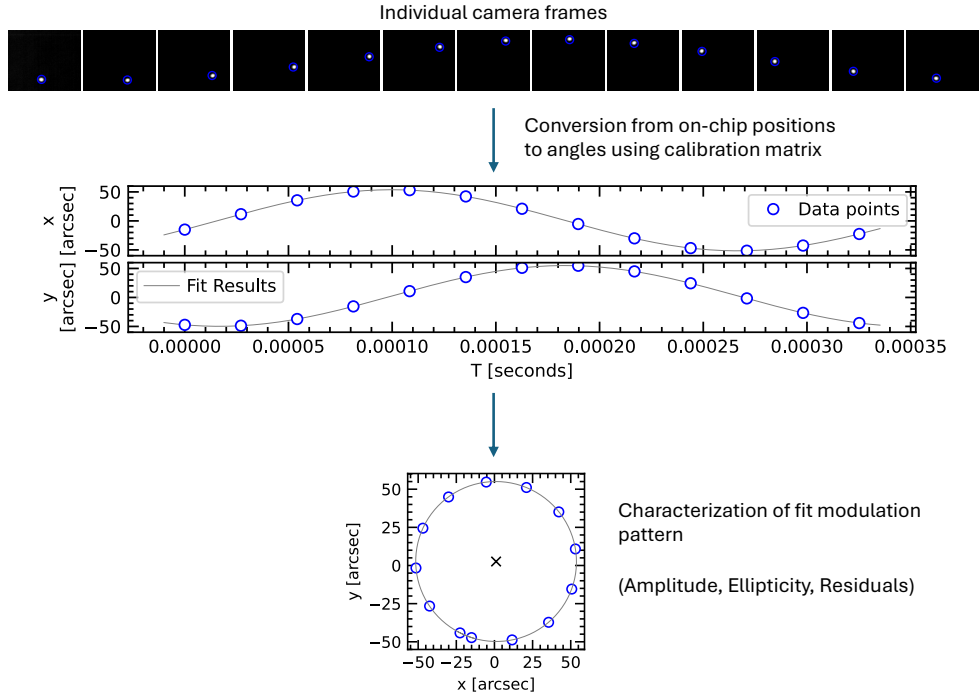


Fig. 5 Illustration of the data reduction process that transforms the time series of images measured with the high speed camera to a time-series of 2D angles.

4.1.1 Centroiding

For each image we start by fitting the LASER spot by fitting a 2-dimensional Gaussian. The central coordinates of the best-fit Gaussian are our best estimate of the on-chip position of the LASER spot. The measured FWHM of the LASER spot is about 5 pixels (4 arcsec). At the highest amplitudes and frequencies it is elongated due to smearing, but even in the most extreme case (Amplitude = 62 arcsec,

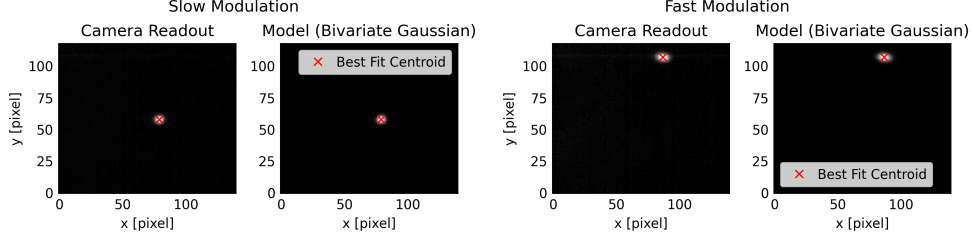


Fig. 6 Illustration how centroids are determined in the individual camera frames by fitting a bivariate Gaussian. Here we show two example images and the best fit model recorded during modulation with low frequencies / amplitudes (*left*) and at the maximum frequency/amplitude (*right*). At high frequencies the LASER spot starts to become elongated, but the centroid is still recovered correctly.

$f = 5000$ Hz) the smearing only reaches 6 pixels due to the short exposure time (3 μ s). The signal-to-noise is high (~ 300) and estimating the centroiding precision with $\sigma_{\text{centroid}} \approx \text{FWHM} / \text{SNR}$ (Lindgren 1978) yields an expected precision of ≤ 0.013 arcsec, similar to what is actually found in the fit residuals at low modulation frequencies (see Appendix A). In Figure 6 we show two example images at different frequencies and the best-fit Gaussian model.

4.1.2 Calibration and fit of modulation pattern

In the next step, we convert the individual on-chip positions to modulator angles using the calibration matrix determined in subsection 3.3. The resulting time-series of 2D angles is then fit with the following parametrization, describing an elliptical modulation pattern with arbitrary rotation:

$$\begin{pmatrix} x \\ y \end{pmatrix} = \begin{pmatrix} A_x \cdot \cos(2\pi \cdot f \cdot (t - t_0)) \\ A_y \cdot \sin(2\pi \cdot f \cdot (t - t_0)) \end{pmatrix} \cdot \begin{pmatrix} \cos \theta & -\sin \theta \\ \sin \theta & \cos \theta \end{pmatrix} + \begin{pmatrix} x_0 \\ y_0 \end{pmatrix} \quad (3)$$

For each amplitude / frequency combination, we store the fit parameters and the statistical properties of the fit residuals. Appendix A shows the measured modulation time series and the residuals of the fit for different amplitudes and frequencies.

4.2 Results

4.2.1 Amplitude of the modulation

From the fit of the measured modulation pattern (see previous section) we can derive several key parameters of the modulation pattern:

First, we determined the mean amplitude $\bar{A} = \frac{1}{2}(A_x + A_y)$ at the different input voltages and frequencies - see Figure 7 (left). At all frequencies, the modulation amplitude shows a linear behaviour with the amplifier input voltage, demonstrating that the desired modulation amplitude can be easily controlled with the voltage. At the same time, the modulation *gain*, i.e. the slope of the relation between input voltage and modulation amplitude, shows an increase with frequency, that can be described by a quadratic function in the probed frequency range - see Figure 7 (right).

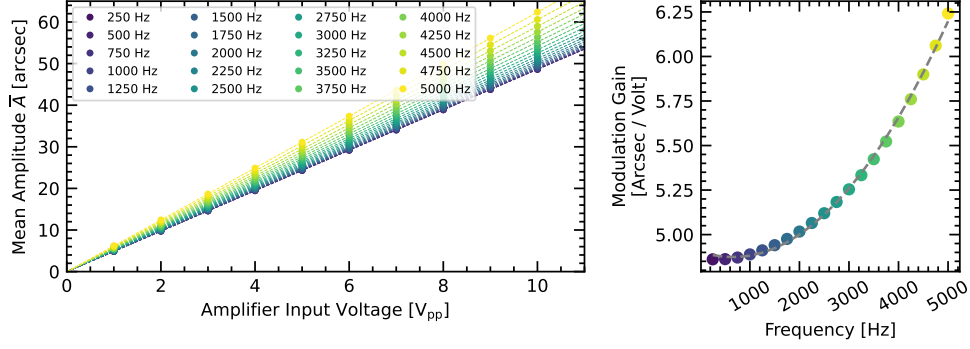


Fig. 7 *Left:* Measured modulation amplitude plotted against input voltage for the 20 different probed frequencies. *Right:* Modulation gain plotted against the frequencies. The dashed line is a 2nd order polynomial fit to the datapoints.

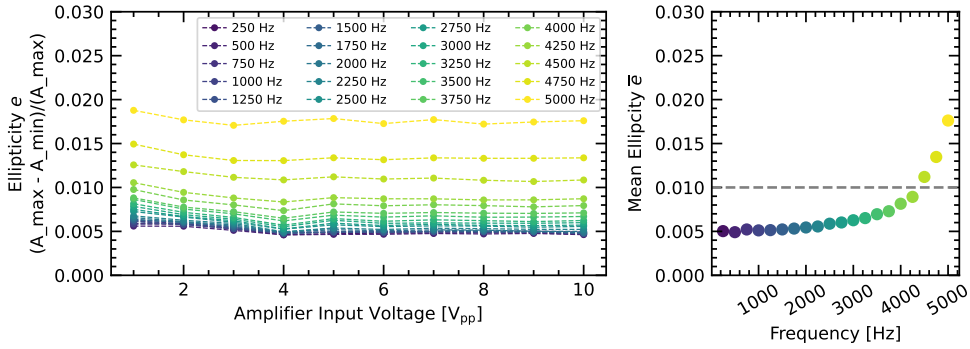


Fig. 8 *Left:* Ellipticity value e plotted against amplifier input voltage for the 20 different probed frequencies. *Right:* Mean ellipticity (averaged over all voltages) plotted against the frequencies.

4.2.2 Ellipticity of the modulation

Ideally, the modulation pattern is perfectly circular. In the next step of the analysis, we study the deviations of the measured modulation from the ideal circular pattern. Figure 8 shows how the ellipticity ($e = \frac{\max(A_x, A_y) - \min(A_x, A_y)}{\max(A_x, A_y)}$) changes with input voltage and frequency. Overall, the ellipticity shows no dependence on the amplifier input voltage and a monotonic increase with modulation frequency. For frequencies from 250 Hz-4250 Hz the ellipticity ranges between 0.005-0.010, after that it increases more steeply with frequency and reaches $e = 0.018$ at 5 kHz.

4.2.3 Non-elliptic deviations of the modulation

Finally, in Figure 9 we study the fit-residuals of the modulation pattern. These residuals are a combination of both our measurement uncertainty and potential additional

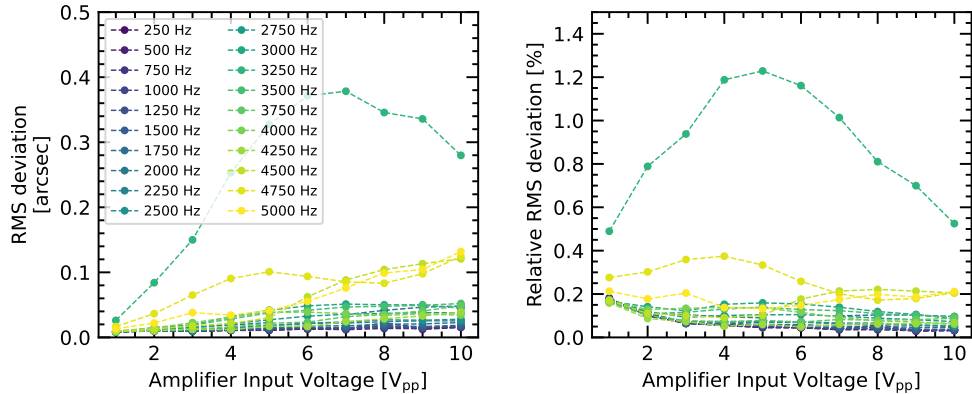


Fig. 9 RMS of modulation residuals after the best-fit elliptical pattern has been subtracted. The *left* plot shows the absolute values, while the *right* plot shows the RMS relative to the respective modulation amplitudes.

(non-elliptical) deviations from the commanded modulation pattern. For most commanded frequencies and amplitudes, the RMS of the fit residuals was below 0.05 arcsec, or 0.2% of the respective modulation amplitude, close to the precision of our individual measurements. However, there are notable exceptions: at high frequencies (4500 Hz, 4750 Hz, 5000 Hz) the absolute RMS values reach up to 0.13 arcsec and the relative RMS values reach around 0.3%. In addition, the most extreme deviations can be seen at a frequency of 3250 Hz, where the absolute deviation reaches 0.38 arcsec and the relative deviation reaches around 1.25%. In [Appendix A](#) we show the measured residuals for several illustrative cases. We suspect that this behaviour at particular frequencies is caused by mechanical resonances, that lead to vibrations.

5 Summary and conclusions

Mechanical modulation of the light path is an essential ingredient for pyramid wavefront sensors and currently limited to modulation frequencies ≤ 1 kHz. We have tested a novel modulator prototype capable of frequencies of up to 5 kHz with a dedicated test setup. The modulator showed stable performance even at 5 kHz with a maximum modulation amplitude of 62.4 arcsec ($= 302.5 \mu\text{rad}$) with no measurable heat dissipation.

For frequencies < 4.5 kHz the deviations from a perfectly circular modulation were minimal with a ellipticity $e < 0.010$ and random deviations from the commanded modulation pattern $\text{RMS} < 0.2\%$. At a single frequency (3250 Hz) we measured larger residuals up to an RMS of 0.4 arcsec/ 1.25%, potentially related to mechanical resonances. For future revisions of the prototype it should be explored whether these resonances are internal to the modulation device or also related to its mounting.

Potential future improvements of the modulator prototype could aim to reduce these resonances, by balancing moving parts and optimizing the housing. In addition,

the potential vibrations that the modulator injects into the system should be quantified and, if necessary, mitigated.

For applications in real AO systems, the exact requirements on the mechanical performance, in particular on stability and repeatability of the modulation trajectory, depend on the respective instrument and the optical design involved. Existing instruments, like METIS and SAXO+, do require the trajectory to be repeatable to about 0.4 arcseconds (2 microrad). This requirement is fulfilled by the modulator presented here in all cases, in fact even in the worst case at the 3250 Hz resonance.

6 Future work

We demonstrated stable operation and high modulation accuracy of the HF modulator prototype using a dedicated test setup. In future studies, the prototype could be integrated into AO test-benches to demonstrate its suitability for XAO applications on a system level. In AO simulations of potential future instruments, the influence of the measured deviations from ideal circular modulation should be taken into account and quantified.

It would also be important to quantify possible surface deformations of the modulator mirror at high frequencies.

In addition, the performance of the modulator prototype for other use-cases such as fast tip-tilt correction and non-circular modulation patterns could be explored.

Acknowledgements. We thank the anonymous referee for constructive feedback that improved the presentation of our results.

The data reduction and visualization was performed using the following software packages:

matplotlib (Hunter 2007), numpy (Harris et al. 2020), scipy (Virtanen et al. 2020), IPython (Perez and Granger 2007), skimage-image (van der Walt et al. 2014)

Declarations

The modulator prototype was provided to MPIA by Physik Instrumente (PI) for testing. The authors do not declare any conflict of interest.

Appendix A Plots of modulations measurements and their residuals

The following figures show the measured modulator angles in xy -space (*first column*) and as time-series (*second column*) as well as the residuals of the ellipse fit (*third and forth column*) for two amplitude settings ($5V_{pp}$: Figure A1, $10V_{pp}$: Figure A2) and several selected modulation frequencies. We can make the following observations: At low modulation frequencies ($f \leq 1000$ Hz), the residuals look purely random and are close to the expected measurement noise (0.01 - 0.02 arcsec). The residuals start to increase for higher frequencies, and eventually reach a maximum at 3250 Hz, which is likely a mechanical resonance and shows clear and systematic deviations from an elliptical pattern. At even higher frequencies, the residuals decrease again. We note

that even though the systematic deviations from perfect modulation are clearly visible at high frequencies, their relative amplitude is small (even in the worst case at the resonant frequency it reaches just 1.2%) and, therefore, they are unlikely to negatively effect the performance of a pyramid wavefront sensor.

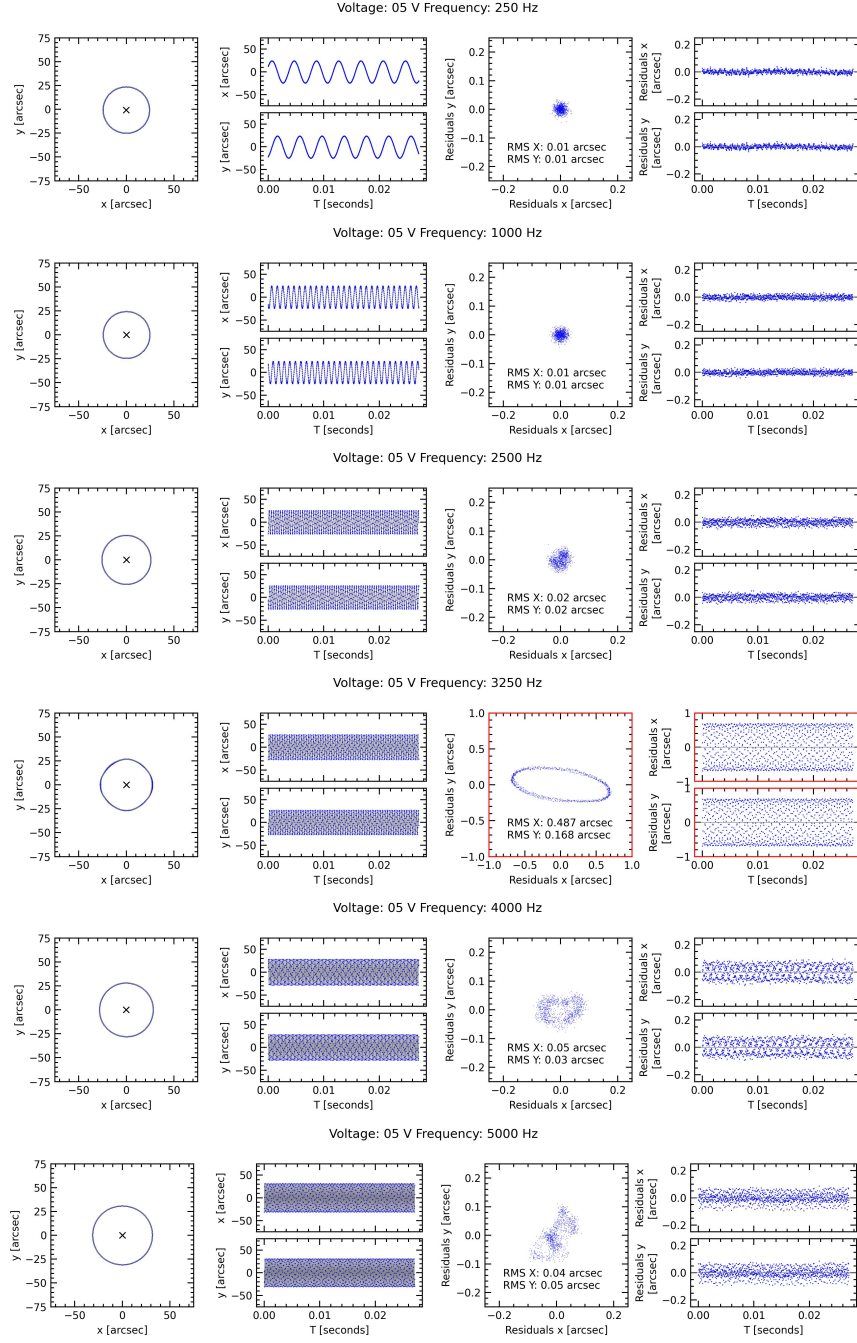


Fig. A1 Measured modulation patterns (*first and second column*) and residuals (*third and fourth column*) from perfect elliptical modulation for six different frequencies and an amplifier input voltage of $5V_{pp}$, corresponding to about half of the maximum probed amplitude. Note the resonant behaviour at 3250 Hz. The different plot scale in the residuals is indicated by red axis spines.

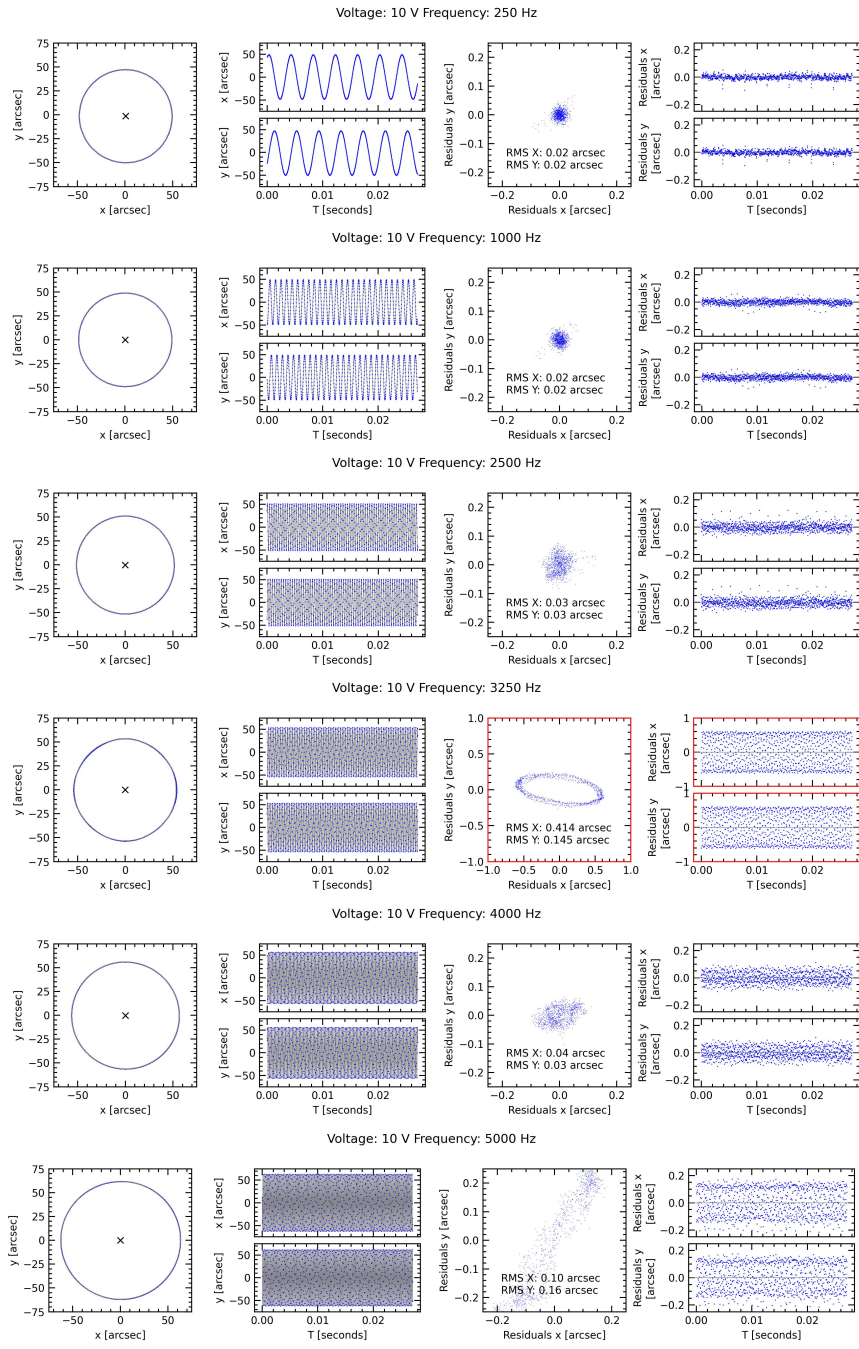


Fig. A2 As [Figure A1](#), but for the maximum probed amplifier input voltage ($10V_{pp}$)

References

- Ammons, S.M., Bauman, B., Burton, G., Gates, C., Dawson, J., Hackel, B., Homoelle, D., Kim, M., Larkin, G., Palmer, D.W., Panas, R., Pax, P., Poyneer, L.A.: LLA-MAS: low-latency adaptive optics at LLNL. In: Close, L.M., Schreiber, L., Schmidt, D. (eds.) *Adaptive Optics Systems VI*. Society of Photo-Optical Instrumentation Engineers (SPIE) Conference Series, vol. 10703, p. 107031 (2018). <https://doi.org/10.1117/12.2314281>
- Boccaletti, A., Chauvin, G., Wildi, F., Milli, J., Stadler, E., Diolaiti, E., Gratton, R., Vidal, F., Loupias, M., Langlois, M., Cantalloube, F., N'Diaye, M., Gratadour, D., Ferreira, F., Tallon, M., Mazoyer, J., Segransan, D., Mouillet, D., Beuzit, J.-L., Bonnefoy, M., Galicher, R., Vigan, A., Snellen, I., Feldt, M., Desidera, S., Rousseau, S., Baruffolo, A., Goulas, C., Baudoz, P., Bechet, C., Benisty, M., Bianco, A., Carry, B., Cascone, E., Charnay, B., Choquet, E., Christiaens, V., Cortecchia, F., Di Caprio, V., De Rosa, A., Desgrange, C., D'Orazi, V., Douté, S., Frangiamore, M., Gendron, E., Ginski, C., Huby, E., Keller, C., Kulcsár, C., Landman, R., Lagarde, S., Lagadec, E., Lagrange, A.-M., Lombini, M., Kasper, M., Ménard, F., Magnard, Y., Malaguti, G., Maurel, D., Mesa, D., Morgante, G., Pantin, E., Pichon, T., Potier, A., Rabou, P., Rochat, S., Terenzi, I., Thiébaud, E., Tallon-Bosc, I., Raynaud, H.-F., Rouan, D., Sevin, A., Schiavone, F., Schreiber, L., Zanutta, A.: Upgrading the high contrast imaging facility SPHERE: science drivers and instrument choices. In: Evans, C.J., Bryant, J.J., Motohara, K. (eds.) *Ground-based and Airborne Instrumentation for Astronomy IX*. Society of Photo-Optical Instrumentation Engineers (SPIE) Conference Series, vol. 12184, p. 121841 (2022). <https://doi.org/10.1117/12.2630154>
- Burvall, A., Daly, E., Chamot, S.R., Dainty, C.: Linearity of the pyramid wavefront sensor. *Opt. Express* **14**(25), 11925–11934 (2006) <https://doi.org/10.1364/OE.14.011925>
- Bond, C.Z., Sauvage, J.-F., Fetick, R., Schwartz, N., Taheri, M., Héritier, C., Morris, T., Fusco, T., Neichel, B., Clarke, F., Thatte, N.: HARMONI at ELT: SCAO performance analysis. In: Jackson, K.J., Schmidt, D., Vernet, E. (eds.) *Adaptive Optics Systems IX*, vol. 13097, p. 130974. SPIE, ??? (2024). <https://doi.org/10.1117/12.3019962>. International Society for Optics and Photonics. <https://doi.org/10.1117/12.3019962>
- Clénet, Y., Buey, T., Gendron, E., Karkar, S., Vidal, F., Cohen, M., Chapron, F., Sevin, A., Thijs, S., Taburet, S., Borgo, B., Huet, J.-M., Blin, A., Dupuis, O., Gaudemard, J., Ferreira, F., Raffard, J., Chemla, F., Lapeyrère, V., Deo, V., Bertrou-Cantou, A., Galland, N., Guieu, S., Meyer, E., Gautherot, N., Tisserand, E., Locatelli, H., Meyer, F., Zidi, A., Kulcsár, C., Raynaud, H.-F., Sassolas, B., Pinard, L., Michel, C., Gratadour, D., Le Ruyet, B., Dembet, R., Ortiz, M., Collin, C., Arslanyan, V., Doncic, B., Ghouchou, L., Ibn Taïeb, I., Baudoz, P., Huby, E., Rousset, G., Rabien, S., Hörmann, V., Sturm, E., Davies, R.: The MICADO first light imager for the ELT: overview of the SCAO module at its final design. In:

- Schreiber, L., Schmidt, D., Vernet, E. (eds.) Adaptive Optics Systems VIII. Society of Photo-Optical Instrumentation Engineers (SPIE) Conference Series, vol. 12185, p. 121854 (2022). <https://doi.org/10.1117/12.2629856>
- Chomez, A., Delorme, P., Lagrange, A.-M., Gratton, R., Flasseur, O., Chauvin, G., Langlois, M., Mazoyer, J., Zurlo, A., Desidera, S., Mesa, D., Bonnefoy, M., Feldt, M., Hagelberg, J., Meyer, M., Vigan, A., Ginski, C., Kenworthy, M., Albert, D., Bergeon, S., Beuzit, J.-L., Biller, B., Bhowmik, T., Boccaletti, A., Bonavita, M., Brandner, W., Cantalloube, F., Cheetham, A., D'Orazi, V., Dominik, C., Fontanive, C., Galicher, R., Henning, Th., Janson, M., Kral, Q., Lagadec, E., Lazzoni, C., Le Coroller, H., Ligi, R., Maire, A.-L., Marleau, G.-D., Menard, F., Messina, S., Meunier, N., Mordasini, C., Moutou, C., Müller, A., Perrot, C., Samland, M., Schmid, H. M., Schmidt, T., Squicciarini, V., Sissa, E., Turatto, M., Udry, S., Abe, L., Antichi, J., Asensio-Torres, R., Baruffolo, A., Baudoz, P., Baudrand, J., Bazzon, A., Blanchard, P., Bohn, A. J., Brown Sevilla, S., Carbillet, M., Carle, M., Cascone, E., Charton, J., Claudi, R., Costille, A., De Caprio, V., Delboulbé, A., Dohlen, K., Engler, N., Fantinel, D., Feautrier, P., Fusco, T., Gigan, P., Girard, J. H., Giro, E., Gisler, D., Gluck, L., Gry, C., Hubin, N., Hugot, E., Jaquet, M., Kasper, M., Le Mignant, D., Llored, M., Madec, F., Magnard, Y., Martinez, P., Maurel, D., Möller-Nilsson, O., Mouillet, D., Moulin, T., Origné, A., Pavlov, A., Perret, D., Petit, C., Pragt, J., Puget, P., Rabou, P., Ramos, J., Rickman, E. L., Rigal, F., Rochat, S., Roelfsema, R., Rousset, G., Roux, A., Salasnich, B., Sauvage, J.-F., Sevin, A., Soenke, C., Stadler, E., Suarez, M., Wahhaj, Z., Weber, L., Wildi, F.: The sphere infrared survey for exoplanets (shine) - iv. complete observations, data reduction and analysis, detection performances, and final results. *A&A* **697**, 99 (2025) <https://doi.org/10.1051/0004-6361/202451751>
- Costa, J.B., Ragazzoni, R., Ghedina, A., Carbillet, M., Vérinaud, C., Feldt, M., Esposito, S., Puga, E., Farinato, J.: Is there need of any modulation in the pyramid wavefront sensor? In: Wizinowich, P.L., Bonaccini, D. (eds.) Adaptive Optical System Technologies II. Society of Photo-Optical Instrumentation Engineers (SPIE) Conference Series, vol. 4839, pp. 288–298 (2003). <https://doi.org/10.1117/12.459032>
- Chambouleyron, V., Wallace, J.K., Jensen-Clem, R., Macintosh, B.: Coronagraph-based wavefront sensors for the high strehl regime. *Opt. Express* **32**(27), 47706–47720 (2024) <https://doi.org/10.1364/OE.539751>
- Davies, R., Kasper, M.: Adaptive Optics for Astronomy. *ARA&A* **50**, 305–351 (2012) <https://doi.org/10.1146/annurev-astro-081811-125447> [arXiv:1201.5741](https://arxiv.org/abs/1201.5741) [astro-ph.IM]
- Engler, B., Kasper, M., Leveratto, S., Heritier, C.T., Bristow, P., Verinaud, C., Louarn, M.L., Nousiainen, J., Helin, T., Bonse, M., Quanz, S., Glauser, A., Gratadour, D., Bernard, J., Clare, R.: The GPU-based High-order adaptive OpticS Testbench. In: Schreiber, L., Schmidt, D., Vernet, E. (eds.) Adaptive Optics Systems VIII,

- vol. 12185, p. 1218558. SPIE, ??? (2022). <https://doi.org/10.1117/12.2630595> . International Society for Optics and Photonics. <https://doi.org/10.1117/12.2630595>
- Feldt, M., Bertram, T., Correia, C., Absil, O., Cárdenas Vázquez, M.C., Coppejans, H., Kulas, M., Obereder, A., Orban de Xivry, G., Scheithauer, S., Steuer, H.: High strehl and high contrast for the ELT instrument METIS: Final design, implementation, and predicted performance of the single-conjugate adaptive optics system. *Experimental Astronomy* **58**(3), 20 (2024) <https://doi.org/10.1007/s10686-024-09968-2> [arXiv:2411.17341](https://arxiv.org/abs/2411.17341) [astro-ph.IM]
- Goulas, C., Galicher, R., Vidal, F., Mazoyer, J., Ferreira, F., Sevin, A., Boccaletti, A., Gendron, E., Béchet, C., Tallon, M., Langlois, M., Kulcsár, C., Raynaud, H.-F., Galland, N., Schreiber, L., Bernardino Dinis, I., Wildi, F., Chauvin, G., Milli, J.: Numerical simulations for the SAXO+ upgrade: Performance analysis of the adaptive optics system. *A&A* **689**, 199 (2024) <https://doi.org/10.1051/0004-6361/202450215> [arXiv:2406.17644](https://arxiv.org/abs/2406.17644) [astro-ph.IM]
- Gillessen, S., Plewa, P.M., Eisenhauer, F., Sari, R., Waisberg, I., Habibi, M., Pfuhl, O., George, E., Dexter, J., von Fellenberg, S., Ott, T., Genzel, R.: An Update on Monitoring Stellar Orbits in the Galactic Center. *ApJ* **837**(1), 30 (2017) <https://doi.org/10.3847/1538-4357/aa5c41> [arXiv:1611.09144](https://arxiv.org/abs/1611.09144) [astro-ph.GA]
- Guzmán, F., Tapia, J., Weinberger, C., Hernández, N., Bacca, J., Neichel, B., Vera, E.: Deep optics preconditioner for modulation-free pyramid wavefront sensing. *Photon. Res.* **12**(2), 301–312 (2024) <https://doi.org/10.1364/PRJ.502245>
- Hartmann, J.: Bemerkungen über den Bau und die Justierung von Spektrographen. *Zeitschrift für Instrumentenkunde* **20** (1900)
- Harris, C.R., Millman, K.J., van der Walt, S.J., Gommers, R., Virtanen, P., Cournapeau, D., Wieser, E., Taylor, J., Berg, S., Smith, N.J., Kern, R., Picus, M., Hoyer, S., van Kerkwijk, M.H., Brett, M., Haldane, A., del Río, J.F., Wiebe, M., Peterson, P., Gérard-Marchant, P., Sheppard, K., Reddy, T., Weckesser, W., Abbasi, H., Gohlke, C., Oliphant, T.E.: Array programming with NumPy. *Nature* **585**(7825), 357–362 (2020) <https://doi.org/10.1038/s41586-020-2649-2> [arXiv:2006.10256](https://arxiv.org/abs/2006.10256) [cs.MS]
- Hutterer, V., Ramlau, R.: Nonlinear wavefront reconstruction methods for pyramid sensors using landweber and landweber–kaczmarz iterations. *Appl. Opt.* **57**(30), 8790–8804 (2018) <https://doi.org/10.1364/AO.57.008790>
- Hunter, J.D.: Matplotlib: A 2D Graphics Environment. *Computing in Science and Engineering* **9**(3), 90–95 (2007) <https://doi.org/10.1109/MCSE.2007.55>
- Kasper, M., Cerpa Urrea, N., Pathak, P., Bonse, M., Nousiainen, J., Engler, B., Heritier, C.T., Kammerer, J., Leveratto, S., Rajani, C., Bristow, P., Le Louarn, M., Madec, P.-Y., Ströbele, S., Verinaud, C., Glauser, A., Quanz, S.P., Helin, T., Keller, C., Snik, F., Boccaletti, A., Chauvin, G., Mouillet, D., Kulcsár, C., Raynaud, H.-F.:

- PCS — A Roadmap for Exoearth Imaging with the ELT. *The Messenger* **182**, 38–43 (2021) <https://doi.org/10.18727/0722-6691/5221> [arXiv:2103.11196](https://arxiv.org/abs/2103.11196) [astro-ph.IM]
- Landman, R., Haffert, S.Y., Long, J.D., Males, J.R., Close, L.M., Foster, W.B., Van Gorkom, K., Guyon, O., Hedglen, A.D., Johnson, P.T., Kautz, M.Y., Kueny, J.K., Li, J., Liberman, J., Lumbres, J., McEwen, E.A., McLeod, A., Schatz, L., Tonucci, E., Twitchell, K.: Making the unmodulated pyramid wavefront sensor smart: II. First on-sky demonstration of extreme adaptive optics with deep learning. *A&A* **696**, 1 (2025) <https://doi.org/10.1051/0004-6361/202553753> [arXiv:2503.16690](https://arxiv.org/abs/2503.16690) [astro-ph.IM]
- Lindgren, L.: Photoelectric Astrometry - a Comparison of Methods for Precise Image Location. In: Prochazka, F.V., Tucker, R.H. (eds.) *IAU Colloquium 48: Modern Astrometry*, p. 197 (1978)
- N'Diaye, M., Vigan, A., Engler, B., Kasper, M., Dohlen, K., Leveratto, S., Floriot, J., Marcos, M., Bailet, C., Bristow, P.: Cascade adaptive optics with a second stage based on a Zernike wavefront sensor for exoplanet observations: Experimental validation on the ESO/GHOST testbed. *A&A* **692**, 157 (2024) <https://doi.org/10.1051/0004-6361/202451449> [arXiv:2411.11946](https://arxiv.org/abs/2411.11946) [astro-ph.IM]
- Perez, F., Granger, B.E.: IPython: A System for Interactive Scientific Computing. *Computing in Science and Engineering* **9**(3), 21–29 (2007) <https://doi.org/10.1109/MCSE.2007.53>
- Ragazzoni, R.: Pupil plane wavefront sensing with an oscillating prism. *Journal of Modern Optics* **43**(2), 289–293 (1996) <https://doi.org/10.1080/09500349608232742>
- Ragazzoni, R., Diolaiti, E., Vernet, E.: A pyramid wavefront sensor with no dynamic modulation. *Optics Communications* **208**(1-3), 51–60 (2002) [https://doi.org/10.1016/S0030-4018\(02\)01580-8](https://doi.org/10.1016/S0030-4018(02)01580-8)
- Schatz, L., Codona, J., Long, J.D., Males, J.R., Pullen, W., Lumbres, J., Van Gorkom, K., Chambouleyron, V., Close, L.M., Correia, C., Fauvarque, O., Fusco, T., Guyon, O., Hart, M., Janin-Potiron, P., Johnson, R., Jovanovic, N., Mateen, M., Sauvage, J.-F., Neichel, B.: Three-sided pyramid wavefront sensor, part II: preliminary demonstration on the new comprehensive adaptive optics and coronagraph test instrument testbed. *Journal of Astronomical Telescopes, Instruments, and Systems* **8**, 049001 (2022) <https://doi.org/10.1117/1.JATIS.8.4.049001> [arXiv:2210.03823](https://arxiv.org/abs/2210.03823) [astro-ph.IM]
- Walt, S., Schönberger, J.L., Nunez-Iglesias, J., Boulogne, F., Warner, J.D., Yager, N., Goullart, E., Yu, T., contributors: scikit-image: image processing in Python. *PeerJ* **2**, 453 (2014) <https://doi.org/10.7717/peerj.453>
- Virtanen, P., Gommers, R., Oliphant, T.E., Haberland, M., Reddy, T., Cournapeau, D., Burovski, E., Peterson, P., Weckesser, W., Bright, J., van der Walt, S.J., Brett,

- M., Wilson, J., Millman, K.J., Mayorov, N., Nelson, A.R.J., Jones, E., Kern, R., Larson, E., Carey, C.J., Polat, İ., Feng, Y., Moore, E.W., VanderPlas, J., Laxalde, D., Perktold, J., Cimrman, R., Henriksen, I., Quintero, E.A., Harris, C.R., Archibald, A.M., Ribeiro, A.H., Pedregosa, F., van Mulbregt, P., SciPy 1.0 Contributors: SciPy 1.0: fundamental algorithms for scientific computing in Python. *Nature Methods* **17**, 261–272 (2020) <https://doi.org/10.1038/s41592-019-0686-2> arXiv:1907.10121 [cs.MS]
- Vérinaud, C., Héritier, C.T., Kasper, M., Tallon, M.: The Bi-O edge wavefront sensor. How Foucault-knife-edge variants can boost extreme adaptive optics. *A&A* **682**, 27 (2024) <https://doi.org/10.1051/0004-6361/202346660> arXiv:2309.07485 [astro-ph.IM]
- Vérinaud, C., Le Louarn, M., Korhikoski, V., Carbillet, M.: Adaptive optics for high-contrast imaging: pyramid sensor versus spatially filtered shack—hartmann sensor. *Monthly Notices of the Royal Astronomical Society: Letters* **357**(1), 26–30 (2005) <https://doi.org/10.1111/j.1745-3933.2005.08638.x>